Overburden deformation induced by dyke-fed conical sandstone intrusions: insights from numerical experiments

Qingfeng Meng[1], David Hodgetts

School of Earth and Environmental Sciences, University of Manchester, Manchester M13 9PL, UK

Abstract

Conical sandstone intrusions, as a distinct type of hydrocarbon reservoirs and carbon sequestration sites, remain poorly understood regarding their emplacement mechanics. Here, we report a numerical modelling study of conical sandstone intrusions using the two-dimensional discrete element method. We built simplified numerical models that contain bonded elastic particles with predefined mechanical properties in an open box as the overburden, and a thin tube filled with unbonded particles as the feeder dyke that is connected to the upper box. The dynamic behavior of the assembly was enabled by displacing of the driving wall that defines the lower boundary of the dyke. The results show that the model composed of soft materials produced a pair of conical, opening-mode fractures in the host sediments as the result of tensile stress concentrations in the fracture tip zones. The overburden deformation was largely localised within the sediments adjacent to the sandbody, without formation of a forced fold and significant uplift of the surface. Differently, the model composed of stiffer materials produced conical fractures that have closed lower segments and opening upper segments with a reverse sense of shear. The intrusion also caused a forced fold in the overburden, with a vertical opening-mode fracture generated in the fold hinge. The modelling results demonstrate that dyke-fed sand intrusions can significantly distort the local

[1] *Corresponding author. E-mail address: meng.qingfeng@hotmail.com

stress field, and the overburden can be subjected to fracturing and/or folding due to differential compaction during gradual inflation of the intrusive sandbody. Moreover, deformation patterns of the overburden in response to sandstone intrusion largely depend on mechanical properties of the host sediments.

Key words

sandstone intrusion; conical; fracture; forced fold; differential compaction

1. Introduction

Sandstone intrusions have been reported in sedimentary basins worldwide (e.g. Hurst and Cartwright, 2007; Polteau et al., 2008; Huuse, 2008; Huuse et al., 2010). In the past two decades, studies of sandstone intrusions have become increasing intensified, mainly because of the use of high-resolution three dimensional (3D) seismic data for subsurface analyses in petroliferous basins that facilitated the identification of reservoir-scale sandstone intrusions (e.g. Cartwright and Huuse, 2005; Huuse et al., 2005, 2007; Cartwright, 2010; Szarawarska et al., 2010). It has been realized that many sandstone intrusions are connected to depositional sandstones as hydrocarbon reservoirs, and thereby have potential economic importance (Huuse et al., 2003a; Hurst et al., 2005, 2006; Lonergan et al., 2000). The intrusive sands, commonly having high porosity and permeability, could form ideal pay zones and add volume to a reservoir at a structurally higher level. Moreover, sandstone intrusions can improve connectivity of reservoirs, and serve as hydraulic conduits for fluid migration (Hurst et al., 2003b; Hurst et al., 2011). However, this could have a negative impact on hydrocarbon accumulations as well. The presence of sandstone intrusions indicates breaches of seals, and can thus degrade the quality of caprocks, whilst oil and gas might escape or be in

communication with another reservoir (Hurst et al., 2003a; Cartwright et al., 2007). More fundamentally, the common occurrence of sandstone intrusions raises important questions regarding the conditions necessary for the development of such structures (Cartwright, 2010).

3D seismic data have demonstrated that large-scale sandstone intrusions, represented as discordant amplitude anomalies, commonly exhibit conical morphologies (Fig. 1a, 1b) that are analogous to many magmatic intrusions (e.g. Molyneux et al., 2002; Omosanya et al., 2017). Such conical sandstone intrusions are exceptionally imaged in the Cenozoic successions throughout the North Sea and the Faeroe-Shetland Basins (Løseth et al., 2003, 2013; Huuse et al., 2004; Huuse and Mickelson, 2004; Shoulders and Cartwright, 2004; Shoulders et al., 2007; Bureau et al., 2013), which can be either sourced from in-situ remoblised depositional sandbodies or from lower-lying sandbodies through dykes (Szarawarska et al., 2010). The emplacement mechanics of conical sandstone intrusions and their geological implications still remain poorly constrained. Some researchers suggested that conical sandstone intrusions could be formed as natural hydraulic fractures under generally Mode I conditions (Fig. 1c) (Jolly and Lonergan, 2002; Cartwright et al., 2008; Vigorito and Hurst, 2010), and the deflection of fracture tips is favored by the development of an asymmetrical stress field in the overburden (Pollard and Johnson, 1973; Hansen and Cartwright, 2006a; McLean et al., 2017). Some other researchers proposed that conical sandstone intrusions may consist of segments of Mode I hydraulic fractures, and also segments of inclined shear fractures as the result of inflating of the intrusive sand body that can cause differential uplifting of the overburden sediments (Fig. 1d) (e.g. Cosgrove and Hillier, 1999; Galland et al., 2009). The shear fractures were subsequently dilated by fluid pressure and filled by fluidized sands. Attempts to address these questions have been relied on scaled analogue experiments (Mathieu et

al., 2008; Galland et al., 2009; Rodrigues et al., 2009; Abdelmalak et al., 2012; Mourgues et al., 2012; Bureau et al., 2014; Montanari et al., 2017; Schmiedel et al., 2017), which could produce intrusion geometries matching those observed in nature. Nevertheless, a more rigorous mechanical analysis of the process of conical sandstone intrusions is still needed in order to improve our understanding of their emplacement mechanism.

Here, we report a numerical modelling study of a specific class of conical sandstone intrusions, i.e. dyke-sourced intrusions, using the discrete element modelling method. In this paper, we first introduce the modelling methodology, followed by characterising the modelling results. Then, we discuss the origin of deformation patterns, and implications for emplacement mechanics of conical -shaped sandstone intrusions. The aims of this paper are (1) to investigate the mechanical interplay between the intrusive sands and the deforming overburden; (2) to refine our understanding of rock mechanical control on deformation patterns; and (3) to investigate the emplacement mechanism of conical sandstone intrusions. The modelling results presented are compatible with many intrusion-related structural features observed in nature, and are believed to provide insights into the development and mechanics of intrusion-related fractures and forced folds, and the mutual interference between sand intrusions and associated overburden deformations. This helps explain the formation conical sandstone bodies and thus has important implications for hydrocarbon exploration and carbon sequestration.

2. Methodology

2.1. The discrete element method

We utilized Particle Flow Code based on the two-dimensional discrete element modelling (DEM) method to construct models in this study. The DEM method was firstly introduced by Cundall and Strack (1979) to simulate the mechanical behavior of a system that consists of a stressed assembly of elastic particles. The general theory of the DEM method described below is mainly summarized from Strayer and Suppe (2002), Benesh et al. (2007), Schöpfer et al. (2007a), and Hughes et al. (2014).

The discrete particles displace independently from one another, and interact only at contacts between the particles. A soft contact approach is used for particle contact, and the particles are allowed to overlap one another at the contacts. The magnitude of particle overlap is determined by the contact force via the force-displacement law. The mechanical behavior of such particles can be then characterised by the movement of each particle and inter-particle forces acting on the particle contacts. The relationship between the particle motion and it driving forces is provided by the Newton's laws of motion. In addition, the particle contacts can be bonded together such that, the particles act as linear-elastic springs in compression, and cohesive bonding that act in both shear and tension (Fig. 2). The contact bond allows tensile stresses to develop at a contact when there is no overlap between neighboring particles. The contact bond is broken when the inter-particle forces acting on any bond exceed the bond strength, which could produce realistic fractures as a result of progressive bond breakage. Movement of particles with unbonded contacts are governed by a frictional strength that resists shear motion. Through-going, macro faults form by the coalescence of adjacent small microfractures.

112 Deformation of a bonded aggregate of particles results from the movement of elastic, frictional
113 walls as the confining boundary for the particles. During deformation, particle interactions are seen
114 as a dynamic process with states of equilibrium developed whenever the internal forces reach a
115 balance. The dynamic process is represented by an explicit timestepping algorithm, which consists
116 of repeated applications of the law of motion to each particle, a force-displacement law to each
117 particle contact, and a constant updating of wall positions. At all times, the forces acting on any
118 particle depend exclusively on its interaction with the contacting particles.
119
120 The DEM method has been used to solve a wide range of problems in granular mechanics. For
121 structural geology and tectonics, the DEM method has been effectively applied to simulate the
122 deformation of upper crustal rock materials, including the development of normal fault (Schöpfer
123 et al., 2006, 2007a, 2007b, 2017; Hardy, 2011, 2013; Smart et al., 2011; Smart and Ferrill, 2018),
124 thrust fault (Strayer and Suppe, 2002; Naylor and Sinclair, 2007; Dean et al., 2013; Morgan, 2015),
125 fracture (Spence and Finch, 2014; Virgo et al., 2014, 2016), strike-slip fault (Imber et al., 2004;
126 Liu and Konietzky, 2018), detachment fold (Hardy and Finch, 2005; Vidal-Royo et al., 2011;
127 Meng and Hodgetts, 2019), and fault-related fold (Finch et al., 2003; Hardy and Finch, 2006;
128 Benesh et al., 2007; Hardy, 2018). These successful previous applications highlight the
129 appropriateness of the DEM method to investigate the development of faults, fractures and folds
130 associated with sandstone intrusions for this study.
131
132 **2.2. Model setup**
133 Our 2D numerical model consists of elastic, frictional disk-shaped particles and walls, with simple
134 initial and boundary conditions (Fig. 2). The model consists of an open box with two vertical walls

and a floor that contained 20,335 particles as the overburden sediments. The particle radii range from 15 to 25 m, following a uniform distribution, which can help avoid hexagonal close packing of these particles. A vertical tube with a width of 100 m, defined by two side walls and a horizontal wall at bottom, Wd, is located underneath the box and connected to the central part of the floor. Such a design satisfies the generally acknowledged model, in which a relatively thin, vertical dyke acts as the fluid migration pathway and also the feeder of sands for conical sandstone intrusions (Huuse et al., 2004; Cartwright et al., 2008). This model has been adapted for several analogue and numerical modelling studies of sandstone and igneous intrusions (Mathieu et al., 2008; Galland et al., 2009; Bureau et al., 2014; Gorczyk and Vogt, 2018).

The particles in the feeder dyke has a radius range from 5 to 10 m, which also follows a uniform distribution. The smaller size for particles in the dyke allows more particle contacts and a more efficient stress transmission within the system. The particles in the overburden were assigned with a density of 2600 kg/m3. The density for particles in the feeder dyke was assigned a value of 1500 kg/m3 to simulate the mixture of water and sand grains. The whole model was gravitationally loaded by 1 g.

Unlike continuum methods, the discrete element method prevents one from directly ascribing the macroscopic mechanical properties and the desired aggregate characteristics, due to the particle-based nature of the models (Benesh et al., 2007). Instead, we first specified the microscopic parameters to individual particles and their contacts, and then iteratively varied these parameters until the desired macroscopic behavior and characteristics are achieved. The appropriate values of particle stiffness, friction and bond strength were then attained by conducting the numerical

158 equivalent of a biaxial rock mechanics test (Cundall and Strack, 1999), which helped derive the
159 macroscopic mechanical properties (Fig. 3). Trials runs of the rock tests were monitored to
160 evaluate whether the particle assembly showed any nonphysical behavior. In such tests, the
161 synthetic rock sample was loaded in a strain-controlled fashion by displacing the top and bottom
162 walls at a sufficiently slow rate, so as to attain a quasistatic solution. The stresses and strains
163 experienced by the rock sample were determined in a macro-fashion by summing the forces acting
164 upon walls and tracking the relative distance between the walls. The samples were loaded until the
165 axial stress falls below 70% of the peak stress. Following these tests, we selected a particle stiffness
166 (both normal and shear) of 1 x 10^6 N/m and 1 x 10^7 N/m for the overburden, a bond strength (both
167 normal and shear) of 1 MPa, and a friction coefficient of 0.2. The micro-mechanical parameters
168 correspond to a Young's Modulus of 2.18 and 21.82 MPa, and a unconfined compressive strength
169 (UCS) of 0.39 and 2.03 MPa for the bulk rock (Table 1), respectively, to reasonably represent soft
170 and stronger clay sediments (e.g. with a higher content of silts and sands) that commonly appear
171 to act as host for conical sandstone intrusions (Huuse et al., 2004). We chose a particle stiffness of
172 1 x 10^7 N/m for the sand particles, both zero for the particle bond strength and friction coefficient
173 to simulate the non-cohesive, fluidized sand grains.
174
175 The particles were allowed to settle to the bottom of the model and compact under their own weight.
176 Firstly, the particles in the feeder dyke were packed under the force of gravity. Once the mean
177 unbalanced force in the whole particle assembly dropped to a negligible value that indicates the
178 achievement of static equilibrium, the extra particles above the top of the dyke were removed. The
179 trim of the assembly resulted in a small amount of vertical elastic rebound, which elevated the
180 upper surface of the assembly. When the new equilibrium had been achieved, the trimming process

was repeated. This operation was iterated until the assembly reached to the dyke top and was thereby considered to be settled. The particles in the overburden were packed in the upper box, following the same routine. At a critical point when the assembly was trimmed to 3 km high and no more than five particles could be removed at a new equilibrium, the packing process was considered finished.

Colors were applied to the particles in the overburden to produce visible layering for later bedding correlations, however, the assembly was mechanically homogeneous. The driving wall that define the lower boundary of the feeder dyke was advanced at a controlled, upward velocity to displace the particles in the dyke to the upper box to simulate the intrusion process, which can represent the lithostatic condition and lead to deformation in the overburden. Six snapshots were taken during the modelling process for each model. We focused on the morphology of the intrusive body, deformation structures in the overburden and synchronous stress trajectories.

3. Results

3.1. Model 1 (Material 1)

At the early stage of injection, the intrusive sands were accumulated as a sub-rounded laccoliths-like body (Fig. 4). The volumetric expansion of the sand body was achieved by both upward and lateral propagations. This resulted in an intrusion-related compaction in the sediments above the sand body and dramatic decrease in the layer thickness, whilst the upper layers were unaffected. The stress field witnessed a strong stress perturbation in the overburden around the intrusive body from a previously isotropic stress field prior to sand intrusion, which is characterised by tensile stress trajectories aligned in a half circular manner in the outer zones of the sand body (Fig. 5).

Then, a pair of opening-mode fractures simultaneously nucleated in the layer above the propagation front of the sand body at T1. The right fracture propagated upward at a faster rate than the left fracture, and firstly reached the magenta layer at T2. Both fractures propagated by the coalescence of neighboring en echelon fractures that formed sequentially in the areas above the fracture tips. This was achieved by tensile stress concentrations within fracture tip regions that led to continuous fracture propagation. Later on, the sand body gradually splitted into two branches, with upward-tapering tips pointing towards the fractures. This was followed by sand particles entering opening fracture channels. Notably, the fractures occur in a hybrid mode, exhibiting a reverse sense of shear. The orange layer right above the intrusive sands was uplifted to a higher level, whilst the overlying layers were much less affected.

3.2. Model 2 (Material 2)

Initially (T1), a small pile of sand particles were intruded into the overburden, with both lateral and vertical propagations, leading to thinning and folding of the overlying orange layer (Fig. 6). This dramatically influenced the stress field in the overburden, which was represented by compressive stresses dominating the areas adjacent to the intrusive body, whilst the upper zones were dominated by tensile stresses that were arranged in a semicircular manner (Fig. 7). Later on, a pair of opening-mode fractures were nucleated within the central part of the overburden and propagated upward, accompanied with diminishing of tensile stresses in fracture zones. Sub-horizontal dilatational steps were produced in the overlapping tip zones of newly-generated fractures and existing ones. Then, the fractures, which exhibit a hybrid mode with a reverse sense of shear, reached the surface. Because of the accumulation of reverse displacement, the two fractures resulted in scarps on the surface as the hangingwall block were transported upward. A

vertical opening-mode fracture was generated in the hinge zone of the forced fold and propagated downward. Notably, the entire block defined by the two inclined fractures was uplifted and folded during the intrusion, which resembles the process of doming or forced folding as described by Hansen and Cartwright (2006b) and Jackson et al. (2013). Interestingly, two areas at the level of the intrusive sandbody were largely dominated at the final stage of the model.

4. Discussion

4.1. Origin of deformation patterns

4.1.1 Role of differential compaction

Both the models presented produced conical fractures that exhibit a distinctive conical geometry with a well-defined apex, and are compatible with those observed in seismic profiles (Fig. 1a, 1b). The fractures developed by upward and outward propagations, as suggested by Cartwright et al. (2008). Notably, the intrusion-related deformation of the overburden in model 1 is mainly localised in the surrounding rocks around the intrusive body. The surface experienced little folding and uplift, which is consistent with the analogue modelling results of sandstone intrusions (Bureau et al., 2014), and also many seismic observations (Huuse and Mickelson, 2004; Cartwright et al., 2008; Bureau et al., 2013). This is in contrast to model 2, in which forced folding of the overlying rocks and a remarkable amount of surface uplift occurred in response to inflation of the intrusive sandbody (Fig. 6).

The fractures produced in both models exhibit a hybrid-mode with a reverse sense of shear, which were due to volumetric inflation of the intrusive sandbody. Such fractures have been explained as natural hydraulic fractures within the host rock (Cartwright et al., 2008; Mourgues et al., 2012).

Alternatively, the fractures have been suggested to result from self-induced shear failure during sand intrusion (Mathieu et al., 2008). Analogue experiments have demonstrated that many dykes could propagate as a viscous indenter and lead to the formation of shear bands or shear faults in the country rock (Mathieu et al., 2008; Montanari et al., 2017) that allow fludised materials to exploit these faults as it is the mechanically easier option (Weertman, 1980). This can be explained using the simple flexure theory (Goulty and Schofield, 2008), i.e. the differences in longitudinal strain within a flexed overburden above an intrusive body will lead to differential compaction of the encasing sediments, and the formation of fractures would be favoured at edges of the intrusive body where maximum bending occurs (Pollard and Johnson, 1973; Cosgrove and Hillier, 1999). This theory has been adapted to interpret the origin of large-scale conical sandstone intrusions in the North Sea (Huuse et al., 2004).

Although our models produced varied overburden deformation patterns, it is demonstrated that intrusion-induced differential compaction of the encasing sediments indeed played a critical role in the formation of the hybrid fractures, as clearly evident from their reverse displacement. Notably, the extensional regimes on both sides of the intrusive sandbody as shown in model 2 are also possible evidence for the flexure theory discussed above. Hydrofracturing is not favoured to explain origin of the fractures, due to the fact that (1) the fractures would be expected to more likely to occur in Mode I if they were tensional hydraulic fractures; and (2) the distinct conical morphology of fractures do not resemble the common appearance of natural hydraulic fractures that exhibit a wide range of geometries and orientations in homogeneous rocks (Cosgrove, 2001; Meng et al., 2017).

4.1.2. Mechanical control on deformation patterns

One of the main differences in the modeling results of the two models is whether forced fold occurred across the entire overburden above the intrusive sandbody. In model 1, only the limited extent of encasing sediments received intrusion-related compaction and were uplifted, whilst the superficial layers in model 1 were not significantly folded or uplifted. Differently, forced folding of the surface co-exists with conical fractures in model 2 and many other cases (e.g. Cosgrove and Hiller, 2000; Shoulders and Cartwright, 2004). The reason whether forced folding occurs in response to subsurface intrusions remains poorly understood. Schmiedel et al (2017) used analogue modelling to reveal that the host rock strength, i.e. cohesion, plays an important role in the final geometry of intrusions and also extent of surface uplift. It is suggested that a lower host rock cohesion favours the formation of conical fractures and a limited extent of surface deformation during intrusions, whilst a higher cohesion promotes lateral propagation of injectities and a larger extent of surface deformation. Their study demonstrates a strong link between deformation patterns and mechanical properties of the host rock during intrusion of remoblised sandstone.

The models presented here share the same initial and boundary conditions, except the different material stiffness. Hence, the different modelling results depend on the only varying parameter, i.e. rock stiffness. The softer materials support localised deformation within a confined area around the intrusive sandbody through a decrease in the total volume. In contrast, the overburden consisting of stiffer materials can only accommodate the injected sands by folding of the overburden to create essential spaces for the injectites.

295 The different mechanical properties of the host sediments can also proudly influence the local
296 stress fields as shown in Figs 5 and 7, especially the distribution of tensile stress regimes that can
297 determine the occurrence of opening fractures. The lower segments of the inclined fractures in
298 model 2 have closed fractures planes, due to the fact that the areas beneath the neutral surface are
299 dominated by compressive stresses.
300
301 **4.2. Implications for emplacement of conical sandstone intrusions**
302 Based on the modelling results and previous observations of seismic data, two different scenarios
303 of dyke-fed sandstone intrusions and the associated deformation in the overburden are proposed
304 here (Fig. 8).
305
306 If the host sediments predominantly consist of soft clays, the dyke, through which fludised sands
307 are transported from the parent body, will tend to grow radially at a critical point when the fluid
308 pressure drops to be inefficient to drive hydro-fracturing (Fig. 8a). The accumulation of sands
309 leads to inflation of the intrusive sandbody and will result in the formation of conical opening
310 fractures at the propagation front of the sandbody due to differential compaction of the encasing
311 sediments. The conical fractures will propagate upward as sandbody inflation continues. The sand
312 grains will penetrate the clays between the fracture channel and the sandbody, and subsequently
313 fill the entire fracture. It is because that the conical fractures are tensile, the sands are readily stored
314 in the fractures when fluid pressure becomes reduced. Under this condition, surface deformation
315 and forced folding can be rather limited.
316

However, if the host sediments are much stiffer, e.g. have a high content of silts and sands, sandstone intrusion can more likely cause forced folding of the entire overburden (Fig. 8b). Opening fractures can occur above the neutral surface and reach the surface, creating clear scarps. Sub-vertical tensile fractures can be generated due to stretching of the flexed overburden. Notably, when remoblised sands enter the fractures, they will be only preferentially stored in the upper segments of the fractures after fluid pressure drops, because areas of the lower segments of the conical fractures are dominated by compressive stresses and will be likely to be closed.

In both cases, fludised sand grains will exploit the conical fractures as a mechanically easier option. Meanwhile, hydraulic fracturing can still operate at the same time (Mathieu et al., 2008), but the hydraulic fractures may be of a smaller-scale and be more abundant over the crest of the sandbody (Cosgrove and Hiller, 2000).

It is worth mentioning that some other factors that can affect the overburden deformation are not considered, such as mechanical stratigraphy and magnitude of fluid pressure. Further studies are suggested to take considerations of more comprehensive parameters for analysing the origin of conical sandstone intrusions.

5. Conclusions

This study utilized the discrete element method to simulate dyke-fed sandstone intrusions and their associated overburden deformations. We conclude the following:

(1) Differential compaction in the encasing sediments of intrusive sandbody can lead to conical fractures in the overburden.

(2) Soft host sediments favours localised deformation and formation of conical-shaped fractures above the intrusive body, whilst stiff host sediments favours forced folding the surface, formation of closed shear fractures below the neutrual surface, opening hybrid fractues above the neutral surface and pure tensile fractures in the hinge zone of the forced fold.

(3) The opening segments of conical fractures that are dominated by tensile stresses, can serve as preferential storage sites for the fludised sands.

(4) Our study provides new insights into the dyke-fed sandstone intrusion-related overburden deformations, and may assist in the understanding of the mechanism of conical-shaped sandstone intrusions in sedimentary basins.

Acknowledgements

This research was supported by the Sandstone Injection Research Group (SIRG) consortium. We thank Andrew Hurst, Mads Huuse and Emma Finch for proving beneficial suggestions. Nicholas Satur and Oliver Galland are thanked for contributing stimulating suggestions.

References

Abdelmalak, M.M., Mourgues, R., Galland, O., Bureau, D., 2012. Fracture mode analysis and related surface deformation during dyke intrusion: Results from 2D experimental modelling. Earth and Planetary Science Letters 359, 93-105.

Benesh, N.P., Plesch, A., Shaw, J.H., Frost, E.K., 2007. Investigation of growth fault bend folding using discrete element modeling: Implications for signatures of active folding above blind thrust faults. Journal of Geophysical Research: Solid Earth 112, B03S04, doi:10.1029/2006JB004466.

363 Bureau, D., Mourgues, R., Cartwright, J., 2014. Use of a new artificial cohesive material for
364 physical modelling: Application to sandstone intrusions and associated fracture networks.
365 Journal of Structural Geology 66, 223-236.
366 Bureau, D., Mourgues, R., Cartwright, J., Foschi, M., Abdelmalak, M.M., 2013. Characterisation
367 of interactions between a pre-existing polygonal fault system and sandstone intrusions and
368 the determination of paleo-stresses in the Faroe-Shetland basin. Journal of Structural
369 Geology 46, 186-199.
370 Cartwright, J., 2010. Regionally extensive emplacement of sandstone intrusions: a brief review.
371 Basin Research 22, 502-516.
372 Cartwright, J., Huuse, M., 2005. 3D seismic technology: the geological 'Hubble'. Basin Research
373 17, 1-20.
374 Cartwright, J., Huuse, M., Aplin, A., 2007. Seal bypass systems. AAPG Bulletin 91, 1141-1166.
375 Cartwright, J., James, D., Huuse, M., Vetel, W., Hurst, A., 2008. The geometry and emplacement
376 of conical sandstone intrusions. Journal of Structural Geology 30, 854-867.
377 Cosgrove, J.W., Hillier, R.D., 1999. Forced-fold development within Tertiary sediments of the
378 Alba Field, UKCS: evidence of differential compaction and post-depositional sandstone
379 remobilization. Geological Society, London, Special Publications 169, 61-71.
380 Cosgrove, J.W., 2001. Hydraulic fracturing during the formation and deformation of a basin: A
381 factor in the dewatering of low-permeability sediments. AAPG Bulletin 85, 737-748
382 Cundall, P.A., Strack, O.D.L., 1979. A discrete numerical model for granular assemblies.
383 Geotechnique 29, 47-65.
384 Cundall, P.A., Strack, O.D.L., 1999. Particle flow code in 2 dimensions. Itasca consulting group,
385 Inc.

386 Dean, S.L., Morgan, J.K., Fournier, T., 2013. Geometries of frontal fold and thrust belts: Insights
387 from discrete element simulations. Journal of Structural Geology 53, 43-53.
388 Finch, E., Hardy, S., Gawthorpe, R., 2003. Discrete element modelling of contractional fault-
389 propagation folding above rigid basement fault blocks. Journal of Structural Geology 25,
390 515-528.
391 Finch, E., Hardy, S., Gawthorpe, R., 2004. Discrete-element modelling of extensional fault-
392 propagation folding above rigid basement fault blocks. Basin Research 16, 467-488.
393 Galland, O., Planke, S., Neumann, E.-R., Malthe-Sørenssen, A., 2009. Experimental modelling of
394 shallow magma emplacement: Application to saucer-shaped intrusions. Earth and Planetary
395 Science Letters 277, 373-383.
396 Gorczyk, W., Vogt, K., 2018. Intrusion of magmatic bodies into the continental crust: 3-D
397 numerical models. Tectonics 37, 705-723.
398 Goulty, N.R., Schofield, N., 2008. Implications of simple flexure theory for the formation of
399 saucer-shaped sills. Journal of Structural Geology 30, 812-817.
400 Hansen, D.M., Cartwright, J., 2006a. Saucer-shaped sill with lobate morphology revealed by 3D
401 seismic data: implications for resolving a shallow-level sill emplacement mechanism.
402 Journal of the Geological Society 163, 509-523.
403 Hansen, D.M., Cartwright, J., 2006b. The three-dimensional geometry and growth of forced folds
404 above saucer-shaped igneous sills. Journal of Structural Geology 28, 1520-1535.
405 Hardy, S., 2011. Cover deformation above steep, basement normal faults: Insights from 2D
406 discrete element modeling. Marine and Petroleum geology 28, 966-972.
407 Hardy, S., 2013. Propagation of blind normal faults to the surface in basaltic sequences: Insights
408 from 2D discrete element modelling. Marine and Petroleum Geology 48, 149-159.

409 Hardy, S., Finch, E., 2005. Discrete-element modelling of detachment folding. Basin Research 17,
410 507-520.
411 Hardy, S., 2018. Discrete element modelling of extensional, growth, fault-propagation folds. Basin
412 Research, https://doi.org/10.1111/bre.12335.
413 Hardy, S., Finch, E., 2006. Discrete element modelling of the influence of cover strength on
414 basement-involved fault-propagation folding. Tectonophysics 415, 225-238.
415 Hughes, A.N., Benesh, N.P., Shaw, J.H., 2014. Factors that control the development of fault-bend
416 versus fault-propagation folds: Insights from mechanical models based on the discrete
417 element method (DEM). Journal of Structural Geology 68, 121-141.
418 Hurst, A., Cartwright, J., Duranti, D., 2003a. Fluidization structures produced by upward injection
419 of sand through a sealing lithology. Geological Society, London, Special Publications 216,
420 123-138.
421 Hurst, A., Cartwright, J., Huuse, M., Jonk, R., Schwab, A., Duranti, D., Cronin, B., 2003b.
422 Significance of large-scale sand injectites as long-term fluid conduits: evidence from seismic
423 data. Geofluids 3, 263-274.
424 Hurst, A., Cartwright, J.A., Duranti, D., Huuse, M., Nelson, M., 2005. Sand injectites: an emerging
425 global play in deep-water clastic environments. Geological Society, London, Petroleum
426 Geology Conference series 6, 133-144.
427 Hurst, A., Cartwright, J.A., Huuse, M., Duranti, D., 2006. Extrusive sandstones (extrudites): A
428 new class of stratigraphic trap? Geological Society, London, Special Publications 254, 289-
429 300.
430 Hurst, A., Cartwright, J., 2007. Relevance of sand injectites to hydrocarbon exploration and
431 production. AAPG Memoir 87, 1-19.

Hurst, A., Scott, A., Vigorito, M., 2011. Physical characteristics of sand injectites. Earth-Science Reviews 106, 215-246.

Huuse, M., 2008. Sandstone intrusions: Implications for exploration and production. World Oil 229, 87-91.

Huuse, M., Cartwright, J., Hurst, A., Steinsland, N., 2007. Seismic characterization of large-scale sandstone intrusions. AAPG Memoir 87, 21-35.

Huuse, M., Cartwright, J.A., Gras, R., Hurst, A., 2005. Kilometre-scale sandstone intrusions in the Eocene of the Outer Moray Firth (UK North Sea): migration paths, reservoirs and potential drilling hazards. Geological Society, London, Petroleum Geology Conference series, 6, 1577-1594.

Huuse, M., Duranti, D., Guargena, C.G., Prat, P., Holm, K., Steinsland, N., Cronin, B.T., Hurst, N., 2003. Sandstone intrusions: Detection and significance for exploration and production. First Break 21, 15-24.

Huuse, M., Duranti, D., Steinsland, N., Guargena, C.G., Prat, P., Holm, K., Cartwright, J.A., Hurst, A., 2004. Seismic characteristics of large-scale sandstone intrusions in the Paleogene of the south Viking Graben, UK and Norwegian North Sea. Geological Society, London, Memoirs 29, 263-278.

Huuse, M., Mickelson, M., 2004. Eocene sandstone intrusions in the Tampen Spur area (Norwegian North Sea Quad 34) imaged by 3D seismic data. Marine and Petroleum Geology 21, 141-155.

Huuse, M., Jackson, C.A.L., Van Rensbergen, P., Davies, R.J., Flemings, P.B., Dixon, R.J., 2010. Subsurface sediment remobilization and fluid flow in sedimentary basins: an overview. Basin Research 22, 342-360.

455 Imber, J., Tuckwell, G.W., Childs, C., Walsh, J.J., Manzocchi, T., Heath, A.E., Bonson, C.G.,
456 Strand, J., 2004. Three-dimensional distinct element modelling of relay growth and
457 breaching along normal faults. Journal of Structural Geology 26, 1897-1911.
458 Jackson, C.A.L., Schofield, N., Golenkov, B., 2013. Geometry and controls on the development
459 of igneous sill–related forced folds: A 2-D seismic reflection case study from offshore
460 southern Australia. GSA Bulletin 125, 1874-1890.
461 Jolly, R.J.H., Lonergan, L., 2002. Mechanisms and controls on the formation of sand intrusions.
462 Journal of the Geological Society 159, 605-617.
463 Løseth, H., Raulline, B., Nygård, A., 2013. Late Cenozoic geological evolution of the northern
464 North Sea: development of a Miocene unconformity reshaped by large-scale Pleistocene
465 sand intrusion. Journal of the Geological Society 170, 133-145.
466 Løseth, H., Wensaas, L., Arntsen, B., Hovland, M., 2003. Gas and fluid injection triggering
467 shallow mud mobilization in the Hordaland Group, North Sea. Geological Society, London,
468 Special Publications 216, 139-157.
469 Lonergan, L., Lee, N., Johnson, H.D., Cartwright, J.A., Jolly, R.J.H., 2000. Remobilisation and
470 injection in deepwater depositional systems: Implications for reservoir architecture and
471 prediction. Gulf Coast Section SEPM Foundation 20th Annual Bob F. Perkins Research
472 Conference, 515-532.
473 Liu, Y., Konietzky, H., 2018. Particle-based modeling of pull-apart basin development. Tectonics
474 37, 343-358.
475 Mathieu, L., De Vries, B.V.W., Holohan, E.P., Troll, V.R., 2008. Dykes, cups, saucers and sills:
476 Analogue experiments on magma intrusion into brittle rocks. Earth and Planetary Science
477 Letters 271, 1-13.

478 McLean, C.E., Schofield, N., Brown, D.J., Jolley, D.W., Reid, A., 2017. 3D seismic imaging of
479 the shallow plumbing system beneath the Ben Nevis Monogenetic Volcanic Field: Faroe–
480 Shetland Basin. Journal of the Geological Society 174, 468-485.
481 Meng, Q., Hooker, J., Cartwright, J., 2017. Genesis of natural hydraulic fractures as an indicator
482 of basin inversion. Journal of Structural Geology 102, 1-20.
483 Meng, Q., Hodgetts, D., 2019. Combined control of décollement layer thickness and cover rock
484 cohesion on structural styles and evolution of fold belts: A discrete element modelling study.
485 Tectonophysics 757, 58-67.
486 Molyneux, S., Cartwright, J., Lonergan, L., 2002. Conical sandstone injection structures imaged
487 by 3D seismic in the central North Sea, UK. First Break 20, 383-393.
488 Montanari, D., Bonini, M., Corti, G., Agostini, A., Del Ventisette, C., 2017. Forced folding above
489 shallow magma intrusions: Insights on supercritical fluid flow from analogue modelling.
490 Journal of Volcanology and Geothermal Research 345, 67-80.
491 Morgan, J.K., 2015. Effects of cohesion on the structural and mechanical evolution of fold and
492 thrust belts and contractional wedges: Discrete element simulations. Journal of Geophysical
493 Research: Solid Earth 120, 3870-3896.
494 Mourgues, R., Bureau, D., Bodet, L., Gay, A., Gressier, J.B., 2012. Formation of conical fractures
495 in sedimentary basins: Experiments involving pore fluids and implications for sandstone
496 intrusion mechanisms. Earth and Planetary Science Letters 313, 67-78.
497 Naylor, M., Sinclair, H.D., 2007. Punctuated thrust deformation in the context of doubly vergent
498 thrust wedges: Implications for the localization of uplift and exhumation. Geology 35, 559-
499 562.

500 Omosanya, K.O., Johansen, S.E., Eruteya, O.E., Waldmann, N., 2017. Forced folding and complex
501 overburden deformation associated with magmatic intrusion in the Vøring Basin, offshore
502 Norway. Tectonophysics 706, 14-34.
503 Pollard, D.D., Johnson, A.M., 1973. Mechanics of growth of some laccolithic intrusions in the
504 Henry Mountains, Utah, II: bending and failure of overburden layers and sill formation.
505 Tectonophysics 18, 311-354.
506 Polteau, S., Mazzini, A., Galland, O., Planke, S., Malthe-Sørenssen, A., 2008. Saucer-shaped
507 intrusions: Occurrences, emplacement and implications. Earth and Planetary Science Letters
508 266, 195-204.
509 Rodrigues, N., Cobbold, P.R., Løseth, H., 2009. Physical modelling of sand injectites.
510 Tectonophysics 474, 610-632.
511 Schöpfer, M.P.J., Childs, C., Manzocchi, T., Walsh, J.J., Nicol, A., Grasemann, B., 2017. The
512 emergence of asymmetric normal fault systems under symmetric boundary conditions.
513 Journal of Structural Geology 104, 159-171.
514 Schöpfer, M.P.J., Childs, C., Walsh, J.J., 2006. Localisation of normal faults in multilayer
515 sequences. Journal of Structural Geology 28, 816-833.
516 Schöpfer, M.P.J., Childs, C., Walsh, J.J., 2007a. Two-dimensional distinct element modeling of
517 the structure and growth of normal faults in multilayer sequences: 1. Model calibration,
518 boundary conditions, and selected results. Journal of Geophysical Research: Solid Earth 112,
519 B10401, doi:10.1029/2006JB004902.
520 Schöpfer, M.P.J., Childs, C., Walsh, J.J., 2007b. Two-dimensional distinct element modeling of
521 the structure and growth of normal faults in multilayer sequences: 2. Impact of confining

522 pressure and strength contrast on fault zone geometry and growth. Journal of Geophysical
523 Research: Solid Earth 112, B10404, doi:10.1029/2006JB004903.
524 Schmiedel, T., Galland, O., Breitkreuz, C., 2017. Dynamics of sill and laccolith emplacement in
525 the brittle crust: Role of host rock strength and deformation mode. Journal of Geophysical
526 Research: Solid Earth 122, 8860-8871.
527 Shoulders, S.J., Cartwright, J., 2004. Constraining the depth and timing of large-scale conical
528 sandstone intrusions. Geology 32, 661-664.
529 Shoulders, S.J., Cartwright, J., Huuse, M., 2007. Large-scale conical sandstone intrusions and
530 polygonal fault systems in Tranche 6, Faroe-Shetland Basin. Marine and Petroleum Geology
531 24, 173-188.
532 Smart, K.J., Wyrick, D.Y., Ferrill, D.A., 2011. Discrete element modeling of Martian pit crater
533 formation in response to extensional fracturing and dilational normal faulting. Journal of
534 Geophysical Research: Planets 116, E04005, doi:10.1029/2010JE003742.
535 Smart, K.J., Ferrill, D.A., 2018. Discrete element modeling of extensional fault-related monocline
536 formation. Journal of Strucutral Geology 115, 82-90.
537 Spence, G.H., Finch, E., 2014. Influences of nodular chert rhythmites on natural fracture networks
538 in carbonates: an outcrop and two-dimensional discrete element modelling study. Geological
539 Society, London, Special Publications 374, 211-249.
540 Strayer, L.M., Suppe, J., 2002. Out-of-plane motion of a thrust sheet during along-strike
541 propagation of a thrust ramp: a distinct-element approach. Journal of Structural Geology 24,
542 637-650.
543 Szarawarska, E., Huuse, M., Hurst, A., De Boer, W., Lu, L., Molyneux, S., Rawlinson, P., 2010.
544 Three-dimensional seismic characterisation of large-scale sandstone intrusions in the lower

545 Palaeogene of the North Sea: completely injected vs. in situ remobilised sandbodies. Basin
546 Research 22, 517-532.
547 Vidal-Royo, O., Hardy, S., Muñoz, J.A., 2011. The roles of complex mechanical stratigraphy and
548 syn-kinematic sedimentation in fold development: insights from discrete-element modelling
549 and application to the Pico del Águila anticline (External Sierras, Southern Pyrenees).
550 Geological Society, London, Special Publications 349, 45-60.
551 Vigorito, M., Hurst, A., 2010. Regional sand injectite architecture as a record of pore-pressure
552 evolution and sand redistribution in the shallow crust: insights from the Panoche Giant
553 Injection Complex, California. Journal of the Geological Society 167, 889-904.
554 Virgo, S., Abe, S., Urai, J.L., 2014. The evolution of crack seal vein and fracture networks in an
555 evolving stress field: Insights from Discrete Element Models of fracture sealing. Journal of
556 Geophysical Research: Solid Earth 119, 8708-8727.
557 Virgo, S., Abe, S., Urai, J.L., 2016. The influence of loading conditions on fracture initiation,
558 propagation, and interaction in rocks with veins: Results from a comparative Discrete
559 Element Method study. Journal of Geophysical Research: Solid Earth 121, 1730-1738.
560 Weertman, J., 1980. The stopping of a rising, liquid-filled crack in the Earth's crust by a freely
561 slipping horizontal joint. Journal of Geophysical Research: Solid Earth 85, 967-976.

Table 1. Rock mechanical parameters for the overburden of the discrete element models.

Parameter	Material 1	Material 2
Particle stiffness (normal and shear), k (N/m)	1e6	1e7
Bond stiffness (normal and shear), $\bar{k}$ (N/m)	1e6	1e7
Bonding cohesion, $\overline{\sigma_c}$ (MPa)	1.00	1.00
Friction coefficient, μ	0.20	0.20
Young's modulus, E (MPa)	2.18	21.82
Unconfined compressive strength, *UCS* (MPa)	0.39	2.03

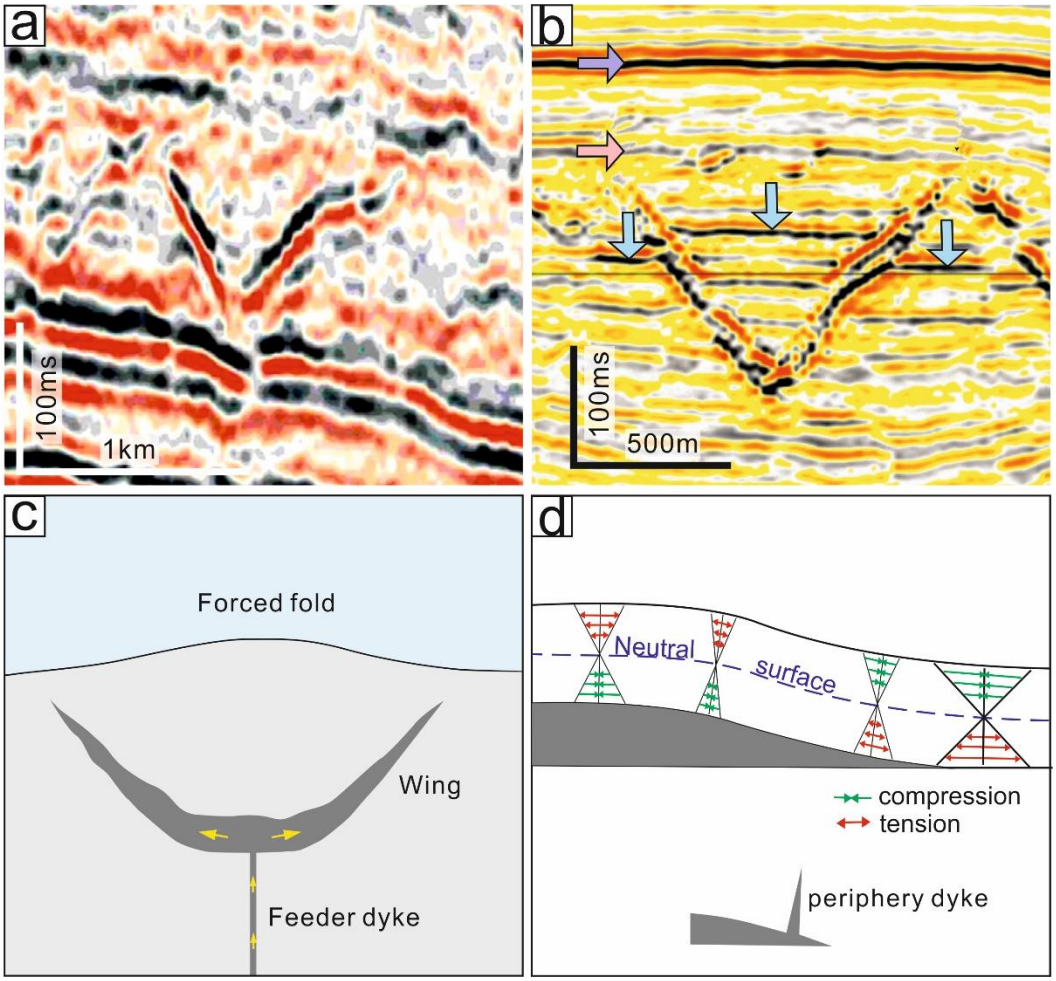

Fig. 1. (a) 2D seismic profiles showing the characteristics of lower Eocene conical amplitude anomaly in the UK North Sea. (from Molyneux et al., 2002). (b) A conical intrusion that has uplifted the flat-topped sediments (vertical arrows) within the cone. Note that the horizons above the conical structure (horizontal arrows) are neither folded, nor uplifted (from Cartwright et al., 2008). (c) Schematic model showing the propagation of conical sandstone intrusions (from Cartwright et al., 2008). (d) Schematic model showing the differences in longitudinal strain within a flexed overburden above an intrusion and origin of periphery dykes along its margin (from Pollard and Johnson, 1973).

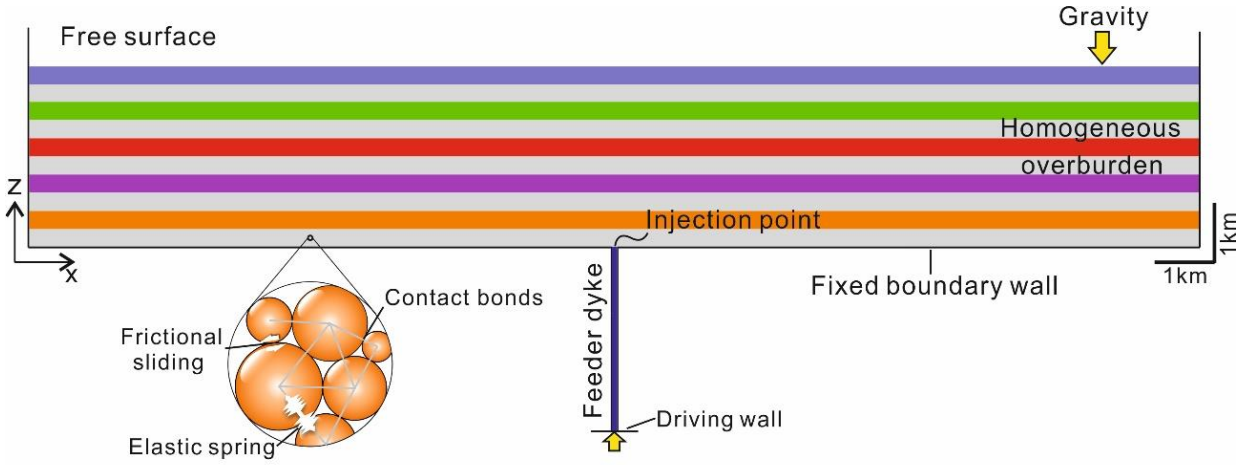

Fig. 2. Schematic illustration showing the geometry and boundary conditions of the model for dyke-fed sand intrusions.

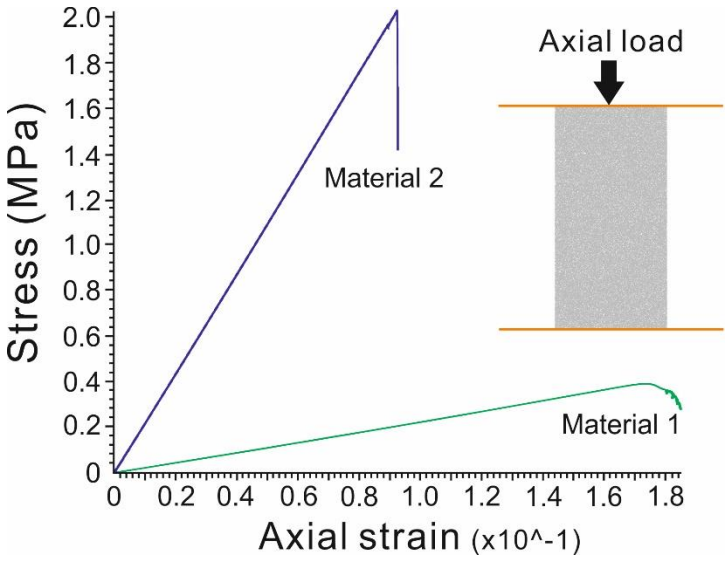

Fig. 3. Plot of stress versus axial strain derived from numerical rock tests. The synthetic rock sample shares the same properties as the intrusion model.

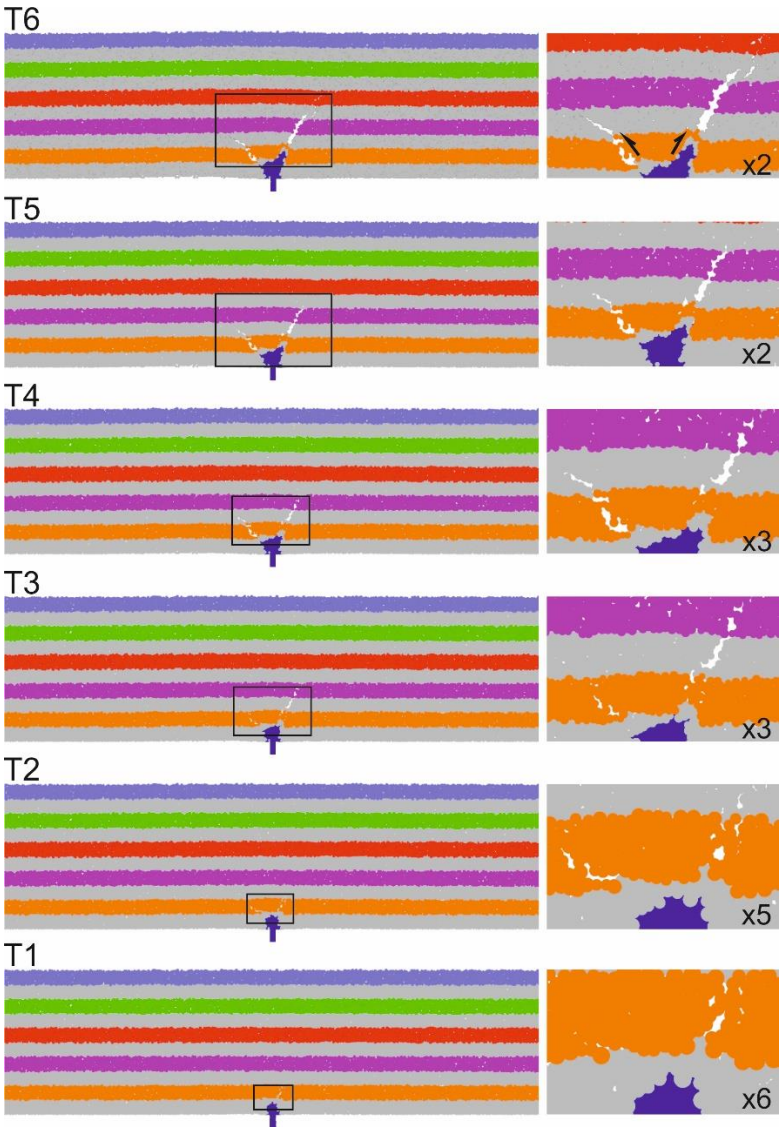

Fig. 4. Snapshots of modelling results of model 1. The enlarged boxes show details of fractures.

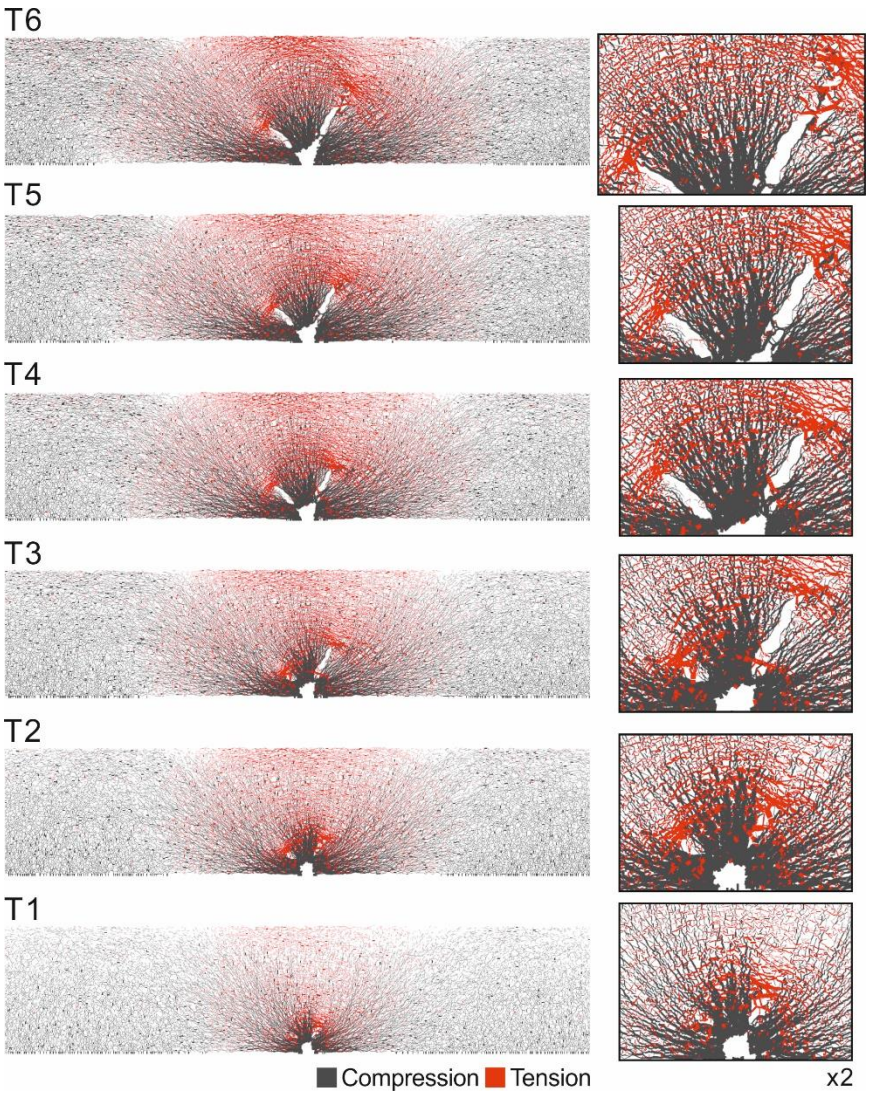

Fig. 5. Snapshots of contact force chains of model 1 showing stress field evolution during inflation of the intrusive sandbody. The enlarged boxes show details of stresses in the fracture zone.

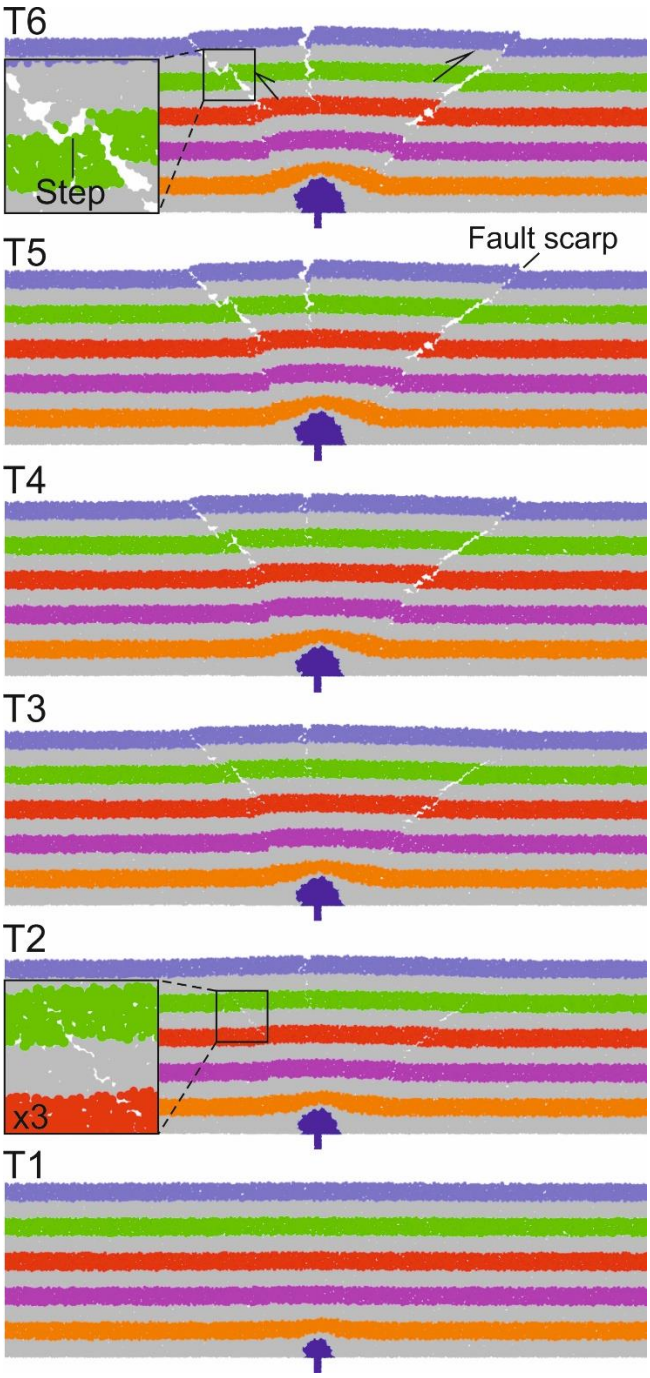

Fig. 6. Snapshots of modelling results of model 2. The enlarged boxes show details of fractures and steps.

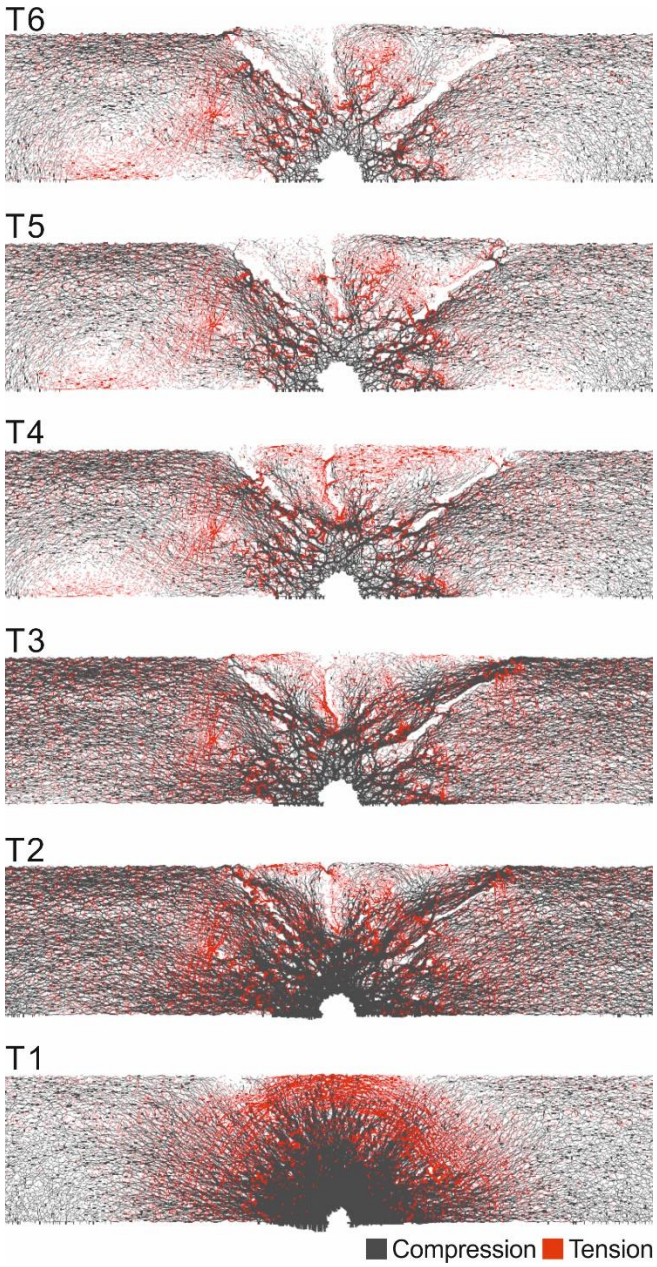

Fig. 7. Snapshots of contact force chains of model 2 showing stress field evolution during inflation of the intrusive sandbody.

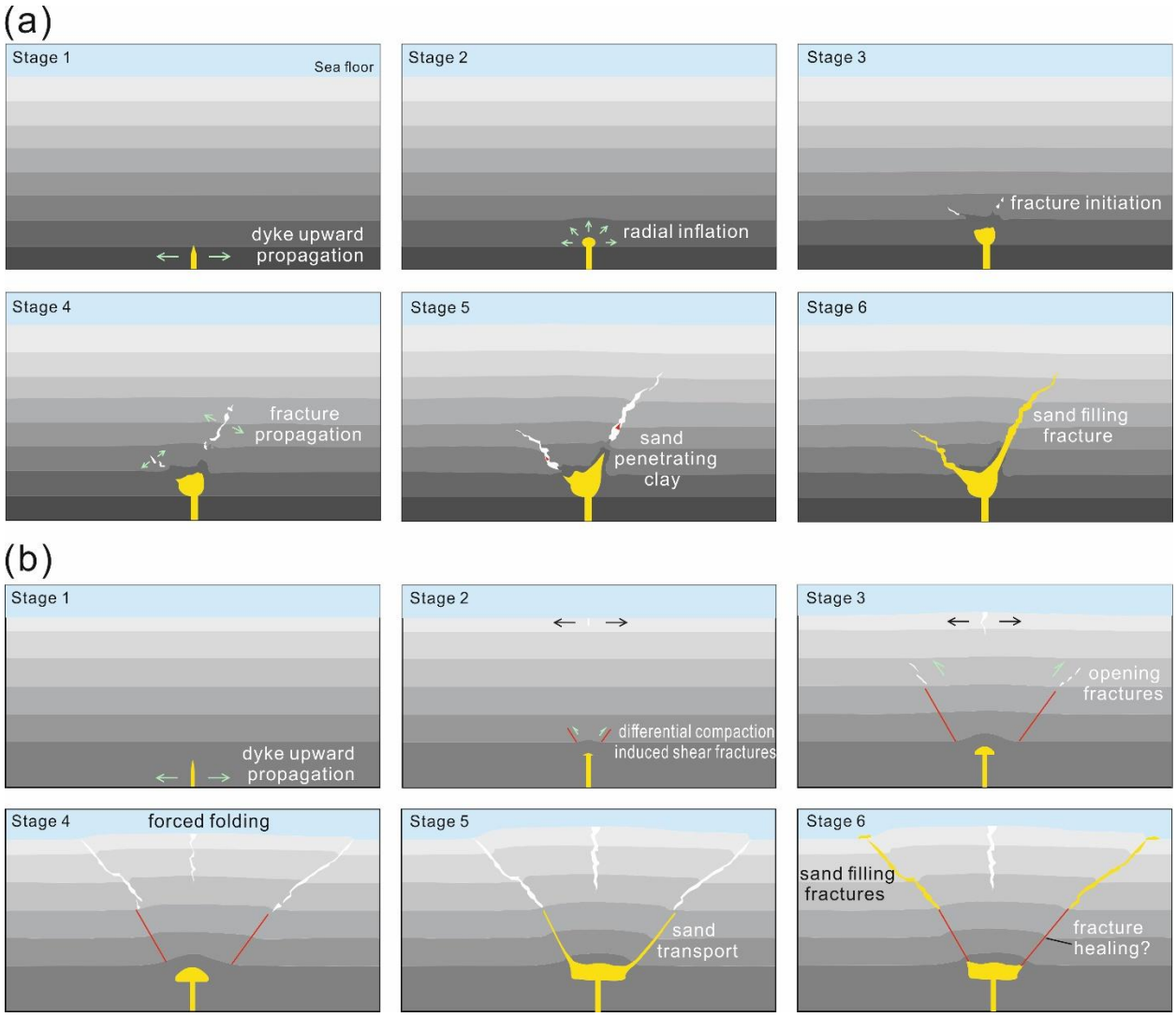

Fig. 8. (a) Schematic model showing the development of conical sandstone intrusions in soft clays. Stage 1, upward propagation of a vertical dyke as a mode 1 hydraulic fracture; Stage 2, lateral propagation of the intrusive body as a laccolith; Stage 3, nucleation of a pair of inclined, opening fractures; Stage 4, continued fracture propagation as the volume of the intrusive body increases; Stage 5, coalescence of dilated voids, resulting in through-going, opening fracture channels that allow the accommodation of mobilized sands; Stage 6, sands penetrating overlying sediments and fully filling the opening-mode fractures. Blue arrows indicate fracture dilation directions. Red arrows indicate directions of sand remobilizations. Yellow color represents sands.

(b) Schematic model showing the development of conical sandstone intrusions in stiff sediments. State 1, upward propagation of a vertical dyke as a mode 1 hydraulic fracture; Stage 2, shear failure induced by differential compaction due to inflation of the intrusive sandbody; Stage 3, nucleation of opening fractures above the neutral surface of the force fold; Stage 4, conical fractures reached the surface; Stage 5, sand transport along the fractures; Stage 6, sand storage in the upper segments of the conical fractures.